(Received 6 February 2026, Accepted 16 March 2026, Scheduled 1 April 2026)

Wideband Circularly Polarized Dielectric Resonator Antenna with Wide Stopband Characteristics

Chuanyun Wang[1,3], Yi Ouyang[1,*], Pin Wen[2], Zhiyong Tan[1], and Tianle Zheng[1]

[1] School of Information Engineering, East China Jiaotong University, Nanchang 330013, China
[2] School of Information Engineering, Nanchang University, Nanchang 330031, China
[3] School of Information and Communications Engineering, Xi'an Jiaotong University, Xi'an 710049, China

ABSTRACT: A wideband circularly polarized (CP) dielectric resonator antenna (DRA) with integrated harmonic suppression is proposed. The design transforms the original rectangular coupled slot into a branched configuration to perturb the electric field distribution within the dielectric resonator (DR) and ground plane, thereby obtaining a wideband circular polarization characteristic. For harmonic suppression, a double-ended feeding structure integrated with a π-shaped stub and a transverse stub is introduced, generating four radiation nulls. Furthermore, a stepped-impedance feeding line is employed to extend the upper stopband bandwidth. A prototype is fabricated and measured; the experimental results and simulations are generally consistent. The antenna achieves a -10 dB impedance bandwidth of 40.2% (2.86–4.3 GHz), a 3 dB axial ratio bandwidth of 26.13% (3.06–3.98 GHz), an average gain of 5.3 dBi, and the harmonic suppression of $2.7f_0$ (where f_0 is the center frequency). The out-of-band suppression in both upper and lower stopbands exceeds 15 dB.

1. INTRODUCTION

The rapid advancement of modern communication systems is driving a growing demand for high-performance antennas. To meet diverse application scenarios, various antenna structures have been extensively investigated. Among them, the ability of circularly polarized antennas to combat multipath fading, reduce polarization mismatch losses, and enhance interference resilience in complex propagation environments makes them highly attractive. Concurrently, radio frequency (RF) front-end technologies are evolving toward higher integration and miniaturization. However, as the number of nonlinear components in the front-end increases, harmonic interference between modules becomes increasingly pronounced. As a key component of the RF chain, the antenna plays a crucial role in system performance. Consequently, developing antennas with wideband harmonic suppression capability is of great practical importance. Furthermore, antennas that simultaneously achieve circular polarization and broadband harmonic suppression not only improve signal reliability and reduce cross-component interference but also facilitate compact and integrated front-end design.

At present, significant research has been conducted on CP antennas [1–7] and antennas with harmonic suppression capabilities [8–14]. Due to their superior anti-interference performance, antennas that integrate both circular polarization (CP) and broadband harmonic suppression have also attracted considerable attention [15–18]. However, conventional microstrip patch antennas face notable limitations, including pronounced conductor and surface wave losses, especially at higher frequencies, as well as inherently narrow bandwidths and relatively large footprints at lower frequencies. Furthermore, such designs typically exhibit limited axial ratio (AR) bandwidth. These constraints restrict their applicability in modern compact and wideband systems, highlighting the need for alternative antenna topologies that can overcome these challenges while maintaining dual functionality in polarization purity and harmonic rejection. Dielectric resonator antennas (DRAs) have garnered extensive research interest owing to their attractive features, including multi-mode operation, high design flexibility, high radiation efficiency, and surface-wave excitation. Leveraging these inherent advantages, CP DRAs have also been widely investigated [19–22]. However, the research on DRAs with harmonic suppression remains relatively limited [23–26], and designs that simultaneously achieve both circular polarization and wideband harmonic suppression are even scarcer. Therefore, developing a DRA that combines CP radiation with broadband harmonic suppression holds considerable practical significance, as it would enhance anti-interference capability and facilitate integration in advanced front-end systems.

The proposed antenna design is primarily divided into two parts: wideband circular polarization and wide harmonic suppression. The conventional rectangular coupling slotline is modified into a branched coupling slotline, serving two main purposes. Firstly, it acts as a coupling structure to feed the dielectric resonator (DR), perturbing its electric field to excite a pair of orthogonal DR modes (TE^{x}_{111} and TE^{y}_{111}). Secondly, it functions as a radiating structure, exciting a pair of orthogonal slot modes (horizontal slot and vertical slot), thereby broadening both the impedance and axial ratio bandwidths. The circular polarization characteristics are further enhanced by introducing asymmetric grooves on the DR. Additionally, the feed line in-

* Corresponding author: Yi Ouyang (13767966219@163.com).

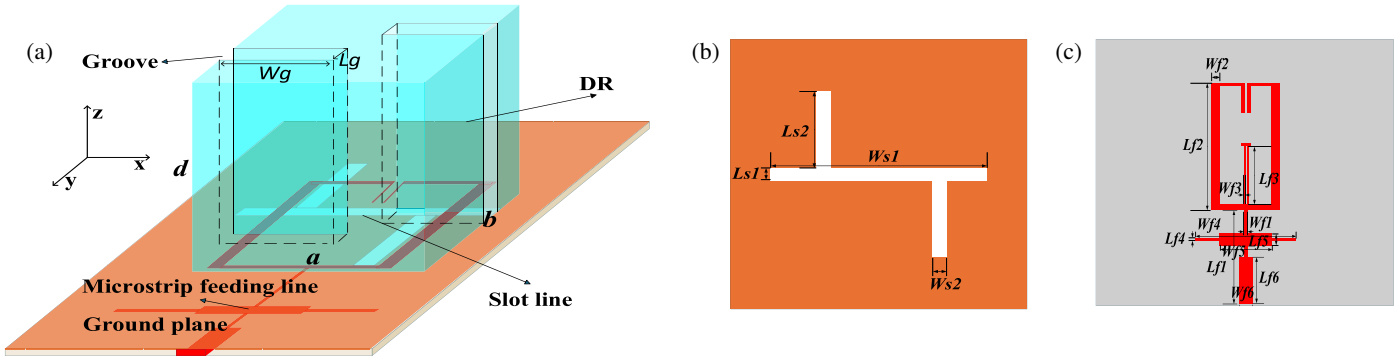

FIGURE 1. Configuration of the proposed DRA. (a) 3-D view. (b) Slot-line view. (c) Feeding-line view.

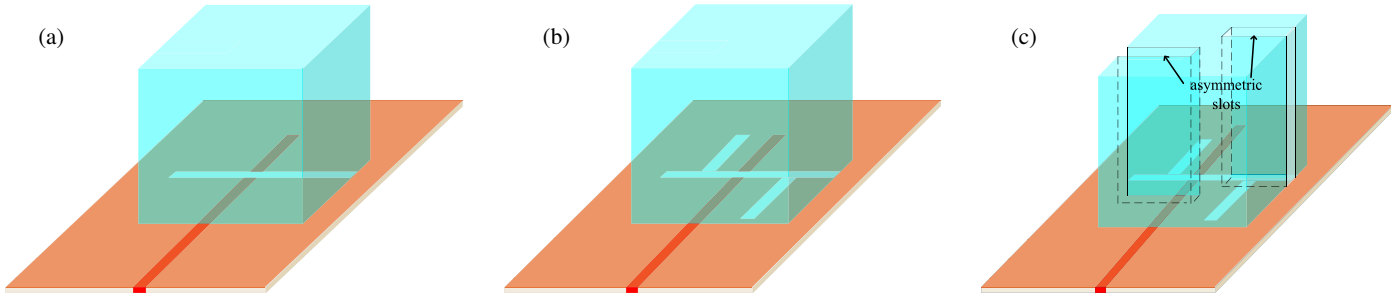

FIGURE 2. Evolution of proposed CP DRA for circular polarization. (a) Antenna I. (b) Antenna II. (c) Antenna III.

corporates a double-ended configuration with a π-shaped stub, a transverse stub, and a stepped-impedance structure, achieving wide harmonic suppression without increasing the antenna's footprint. The proposed antenna covers bands n77 and n78 of 5G, making it suitable for urban public network communication services and Vehicular communication [27].

2. ANTENNA EVOLUTION AND WORKING PRINCIPLE

2.1. Antenna Evolution

The configuration of the proposed wideband CP DRA with harmonic suppression is shown in Fig. 1. The structure consists of four main layers: a grooved dielectric resonator, a slotted ground plane, a dielectric substrate, and a double-ended microstrip feeding line. The dielectric resonator, positioned on the top layer, has lateral dimensions $a * b$, a thickness $d = 16\,\text{mm}$, and material Arlon AD1000 ($\varepsilon_r = 10$, $\tan\delta = 0.023$). Two asymmetric grooves are etched on the resonator to perturb its electric field distribution, thereby facilitating the excitation of orthogonal modes required for circular polarization. Beneath the resonator lies the metal ground plane, which incorporates a branched slot structure. This slot serves dual purposes: On the one hand, it couples energy from the feed network to excite the fundamental mode of the dielectric resonator (DR), thereby perturbing the field to generate the quadrature phase characteristic for CP operation. On the other hand, it serves as a radiator, generating the orthogonal modes of the slot. The ground plane is supported by a dielectric substrate with dimensions $L_1 = 40\,\text{mm}$, $W_1 = 40\,\text{mm}$, thickness $H_1 = 0.762\,\text{mm}$, and material FR4 ($\varepsilon_r = 4.4$, $\tan\delta = 0.02$). On the bottom layer, the feed network is implemented. It comprises a double-branch feeding line integrated with a π-shaped stub and a transverse stub. This configuration introduces multiple radiation nulls, which suppress higher-order harmonics and improve out-of-band selectivity. Additionally, a stepped-impedance section is incorporated into the feeding line to extend harmonic suppression to higher frequencies, thereby widening the overall stopband. The key design parameters are summarized in Table 1.

TABLE 1. Main design parameters of antenna (mm).

a	b	d	L_g	W_g	L_{s1}	W_{s1}
21	21	16	3	11.5	1.1	12.5
L_{s2}	W_{s2}	L_{f1}	W_{f1}	L_{f2}	W_{f2}	L_{f3}
7.4	1.2	12.4	0.1	11.3	0.7	7
W_{f3}	L_{f4}	W_{f4}	L_{f5}	W_{f5}	L_{f6}	W_{f6}
0.1	0.1	14.3	0.4	8.8	5	1.9

2.2. Realization and Working Principle of Wideband Circular Polarization

To mitigate multi-path fading interference during signal propagation, the proposed antenna is designed to transition from linear polarization to circular polarization. The development and final performance of the CP antenna are summarized in Fig. 2 and Fig. 3, respectively. Antenna I exhibits no circular polarization tendency since the axial ratio (AR) is significantly greater than 3 dB and possesses a relatively narrow impedance bandwidth, supporting only the fundamental TE^{y}_{111} mode of dielectric resonator and slot mode.

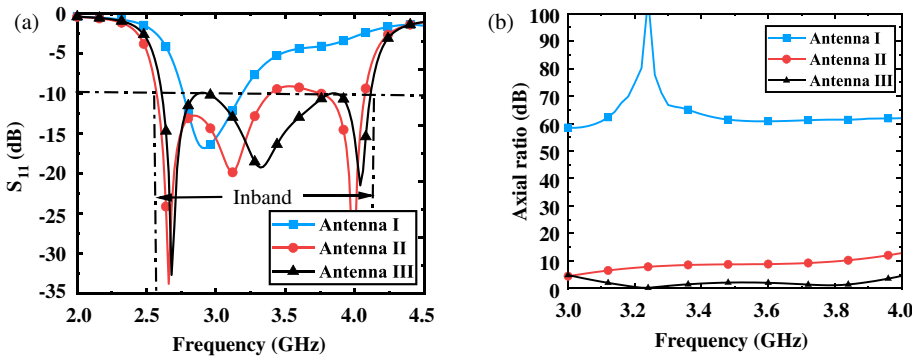

FIGURE 3. Simulated S_{11}, axial ratio of the reference and proposed antennas. (a) S_{11}. (b) Axial ratio.

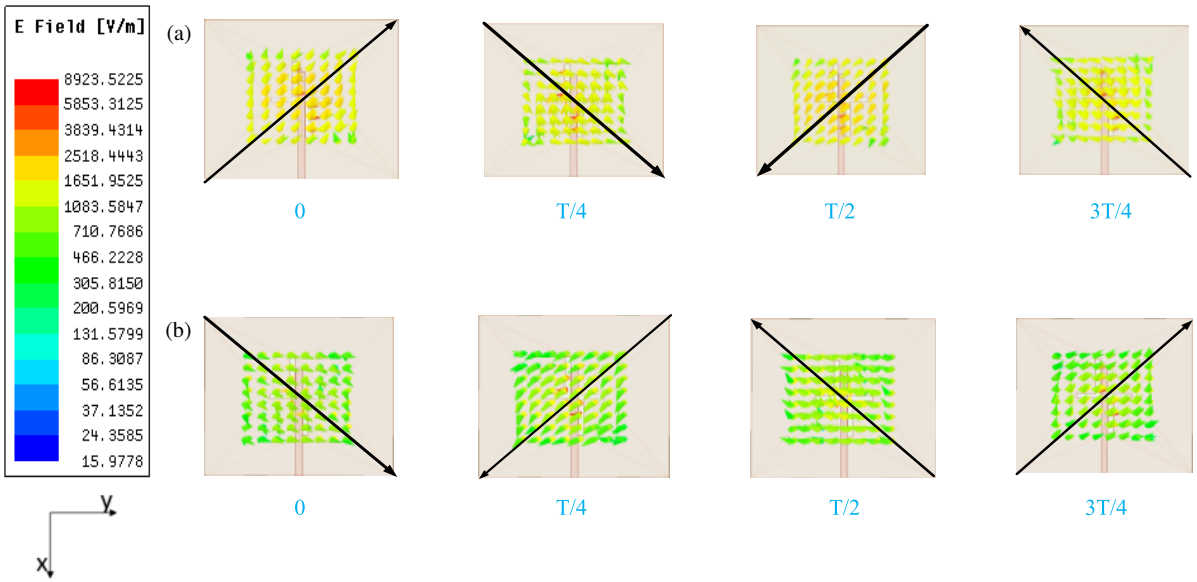

FIGURE 4. The surface electric field distribution of DR at different times. (a) 3.24 GHz. (b) 3.78 GHz.

To introduce circular polarization, branched slotlines are incorporated in Antenna II. These slots not only reshape the electric field to excite orthogonal TE^{x}_{111} and TE^{y}_{111} modes of dielectric resonator, enabling left-handed circular polarization (LHCP) radiation since the axial ratio (AR) has decreased to nearly 3 dB, but also excite additional modes from the branched slots, thereby extending the impedance bandwidth and AR bandwidth. However, the AR of Antenna II remains unsatisfactory since the axial ratio in the passband is still higher than 3 dB. To improve circular polarization performance, two asymmetric grooves are added on each side of the dielectric resonator in the final design, as we can see in Antenna III. These grooves further remold the electric field, enhancing the circular polarization characteristic because the AR drops below 3 dB. As observed in Fig. 3(b), two AR nulls appear at 3.24 GHz and 3.78 GHz, effectively broadening the AR bandwidth. To further elucidate the circular polarization mechanism, Fig. 4 presents the surface electric field distributions on the dielectric resonator at 3.24 GHz and 3.78 GHz at different times. At both frequencies, the surface electric field rotates clockwise over one period, confirming the generation of LHCP radiation. Furthermore, to explain the generation mechanism of multi-mode circular polarization, we simulated the characteristic modes of the branched slotline and the dielectric resonator (DR) with asymmetric grooves. The results indicate that when the branched slotline is introduced, two modes can be generated at 2.86 GHz and 3.88 GHz. Figs. 5(a) and (b) illustrate the electric field distributions of these two slotline modes, respectively. It can be observed that the electric field at 2.86 GHz is primarily concentrated on the horizontal slotline, while the electric field at 3.88 GHz is mainly concentrated on the vertical slotline. Moreover, the electric fields of these two modes are orthogonal, providing favorable conditions for achieving circular polarization. Meanwhile, Figs. 5(c) and (d) display the electric field distributions of the DR's characteristic modes at 3.02 GHz and 3.72 GHz. Two grooves are introduced to perturb the DR's electric field, and the TE_{111} mode of the DR splits into a pair of orthogonal modes. As evident from the DR's electric field distribution, the field at 3.02 GHz is predominantly horizontally oriented, corresponding to the DR's TE^{x}_{111} mode, while the field at 3.72 GHz is mainly vertically oriented, corresponding to the DR's TE^{y}_{111} mode. The integration of these two pairs of orthogonal modes enables a wide impedance bandwidth and a broad axial ratio bandwidth.

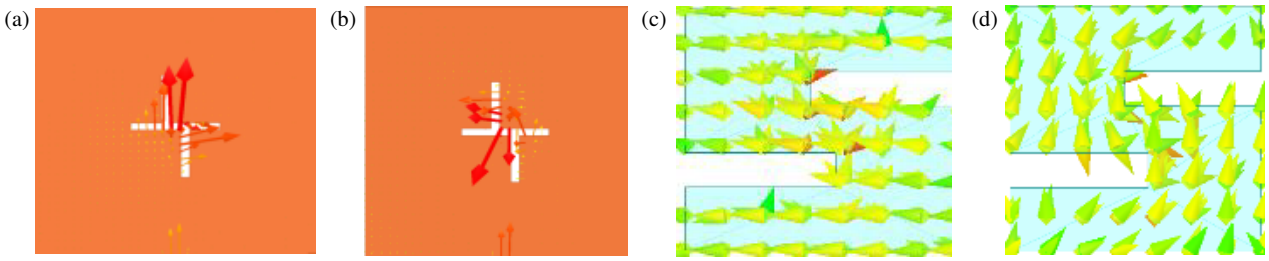

FIGURE 5. Electric field in degenerate modes of DR and slotline. (a) 2.86 GHz, (b) 3.88 GHz, (c) 3.02 GHz, (d) 3.72 GHz.

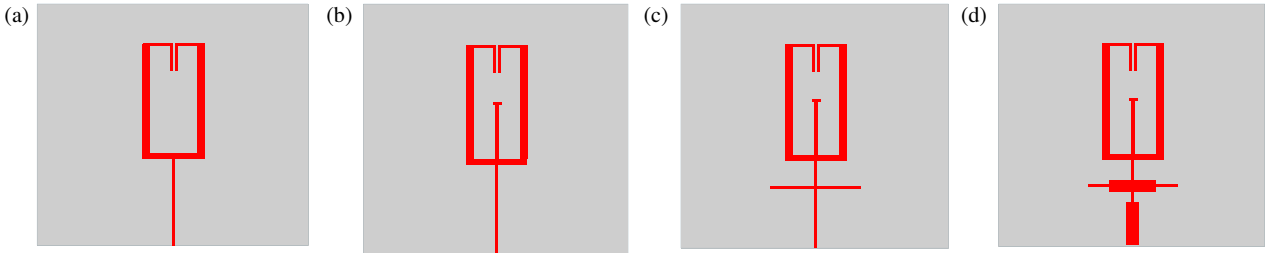

FIGURE 6. Evolution of antenna design for harmonic suppression. (a) Antenna I, (b) Antenna II, (c) Antenna III, (d) Antenna IV.

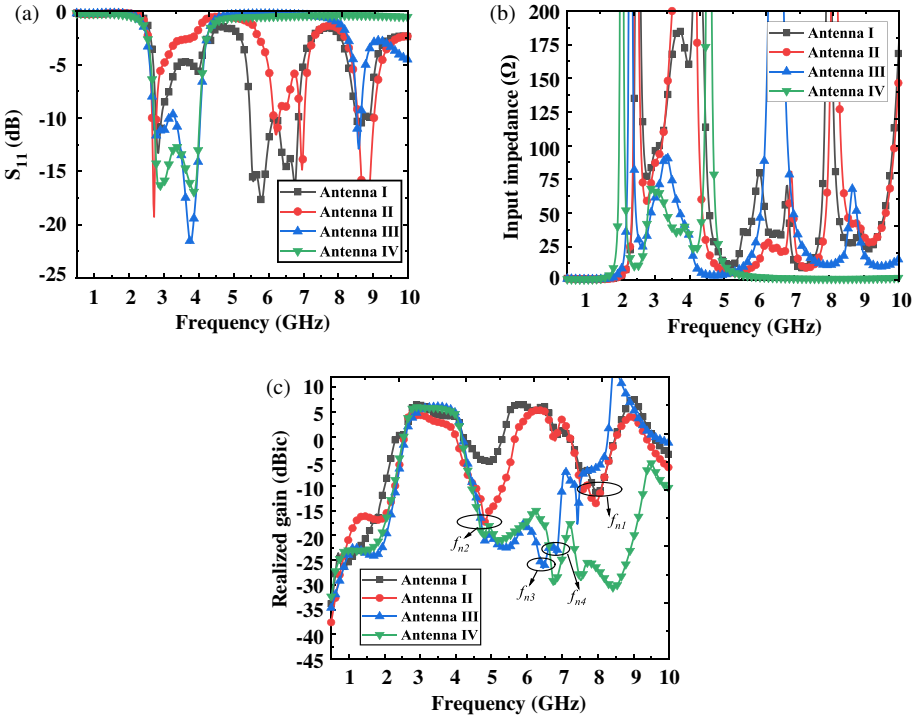

FIGURE 7. The evolutionary process results of antenna design for harmonic suppression. (a) S_{11}. (b) Input impedance. (c) Realized gain.

2.3. Realization and Working Principle of Harmonic Suppression

To suppress harmonic interference and enhance the purity of circularly polarized radiation, a harmonic suppression mechanism is integrated into the antenna design without increasing its footprint. This section details the design process and operational principle of the harmonic suppression technique. A series of harmonics is observed in the upper stopband of the original wideband circularly polarized (CP) antenna. Some innovative modifications were made to the feeding line to obtain harmonic suppression. Since all wide harmonic suppression components are designed within the feedline, while the wideband circular polarization section remains the same, only the feedline design is shown in Fig. 6. As illustrated in Fig. 6(a), the original rectangular microstrip feeding line is redesigned as a double-ended feeding structure in Antenna I, thereby introducing the first radiation null at 7.8 GHz (f_{n1}), as shown in Fig. 7(c). Also, as shown in Fig. 7(b), it lowers input impedance near the radiation

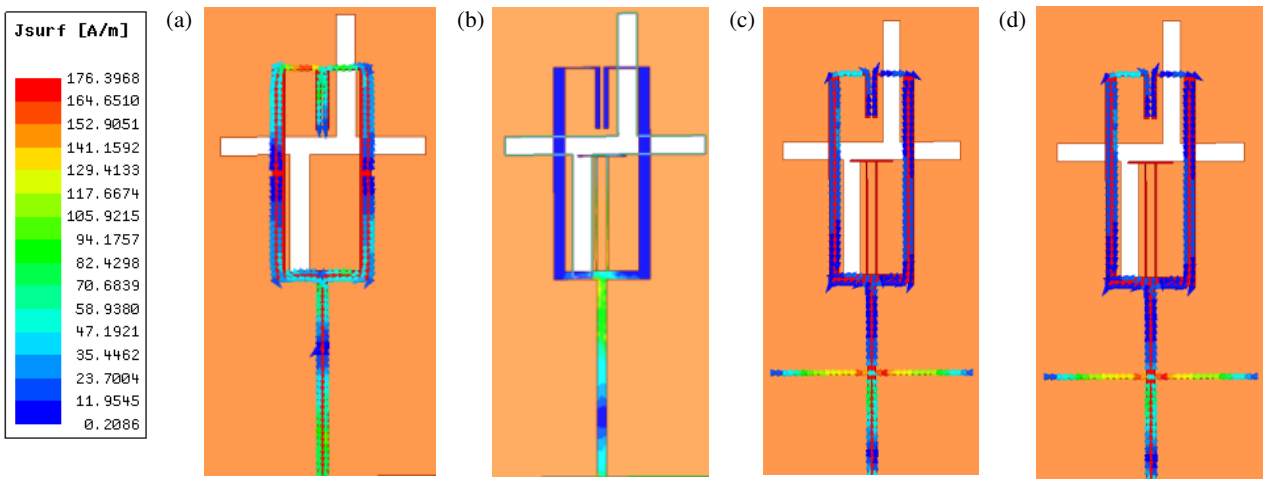

FIGURE 8. The surface current of radiation nulls at different frequencies of the feeding line. (a) 7.8 GHz, (b) 4.82 GHz, (c) 6.46 GHz, (d) 6.82 GHz.

null (f_{n1}), consequently mismatching the harmonics nearby. As illustrated in Fig. 6(b) and Fig. 7(c), a π-shaped stub is incorporated in Antenna II, introducing the second radiation null at 4.82 GHz (f_{n2}), which enhances the out-of-band suppression of the upper stopband, simultaneously suppressing the harmonics with an anomalous radiation pattern around this null. As observed in Fig. 7(a), there are still several harmonics in Antenna III. To address this, a transverse stub is introduced in Antenna III, thereby generating another two radiation nulls at 6.46 GHz (f_{n3}) and 6.82 GHz (f_{n4}), as displayed in Fig. 7(c), which not only mismatch the remaining harmonics but also improve the in-band impedance matching, as confirmed by Antenna III in Figs. 7(a) and (b). Finally, in Antenna IV, to further extend the stopband, a stepped-impedance resonator (SIR) structure is incorporated, inducing the left harmonics around 9 GHz impedance mismatch, thereby establishing a wide stopband ranging 0.1–2.8 GHz and 4.3–10 GHz. Since the four generated nulls are realized step by step, all within the feedline, the loading effect of the stubs during the introduction of subsequent nulls may cause slight shifts to the existing nulls.

The formation mechanism of the four radiation nulls is examined through an analysis of the surface current distributions on the feeding structure as presented in Fig. 8. At the first radiation null ($f_{n1} = 7.8$ GHz, Fig. 8(a)), surface current is concentrated primarily on the transverse segment of the double-ended feed line with inverted phase, leading to far-field cancellation. At the second radiation null ($f_{n2} = 4.82$ GHz, Fig. 8(b)), the strong surface current is largely confined to the π-shaped stub. Consequently, minimal energy is coupled through the slot to the dielectric resonator (DR), resulting in weak radiation. The surface currents at the third and fourth radiation nulls ($f_{n3} = 6.46$ GHz and $f_{n4} = 6.82$ GHz) are shown in Figs. 8(c) and (d). In both cases, energy is strongly localized on the transverse stub, with little transmitted through the coupling slot to DR. The phase-opposed currents on this stub cause radiation cancellation, resulting in weak radiation. Moreover, four radiation nulls are tunable, as demonstrated by the parametric study in Fig. 9.

2.4. Parameter Analysis

A comprehensive parametric study was performed to validate the structural reliability and design flexibility of the proposed antenna. The influence of key geometric parameters on impedance matching (S_{11}), axial ratio (AR), and radiation nulls of realized gain are analyzed below.

Specifically, as illustrated in Fig. 9(a), as the length of W_{s1} increases from 12.5 mm to 16.5 mm, Mode I shifts towards lower frequency while the remaining three modes affect only impedance variations with no observable frequency shift. As shown in Fig. 9(b), as the vertical slot length L_{s2} rises from 6.4 mm to 8.4 mm, Mode I and Mode IV show a clear downward shift in frequency together. The consistent frequency shift of these two modes is because the lengths of the current paths are both affected with varying L_{s2}. Meanwhile, as displayed in Fig. 9(c), as DR height d varies from 14 mm to 18 mm, Modes II and III drift downward in frequency, while Modes I and IV remain fixed in frequency, altering only in impedance. As shown in Fig. 9(d), as the asymmetric slot depth W_g extends from 7.5 mm to 11.5 mm, the minimum AR point shifts toward higher frequency. It can be concluded that Mode I and Mode IV are associated with the horizontal and vertical slots, respectively, while Mode II and Mode III correspond to the orthogonal modes of TE^x_{111} and TE^y_{111} of the dielectric resonator (DR).

Furthermore, the frequency of the axial ratio minimum point can be effectively controlled through parametric adjustment. The parametric analysis of the four radiation nulls is also presented in Fig. 10. As illustrated in Fig. 10(a), when the length of the double-ended feed line L_{f2} increases from 12.3 mm to 13.3 mm, the frequency of the first radiation null f_{n1} (7.8 GHz) monotonically decreases towards low frequency, proving the controllability. As depicted in Fig. 10(b), as the length of the π-shaped stub L_{f3} ranges from 7.0 mm to 7.4 mm, the frequency of the second radiation null f_{n2} (4.82 GHz) decreases. The influence of the transverse stub length W_{f4} on the third and fourth radiation nulls (f_{n3} at 6.46 GHz and f_{n4} at 6.82 GHz) is illustrated in Fig. 10(c). Both nulls exhibit a simultaneous

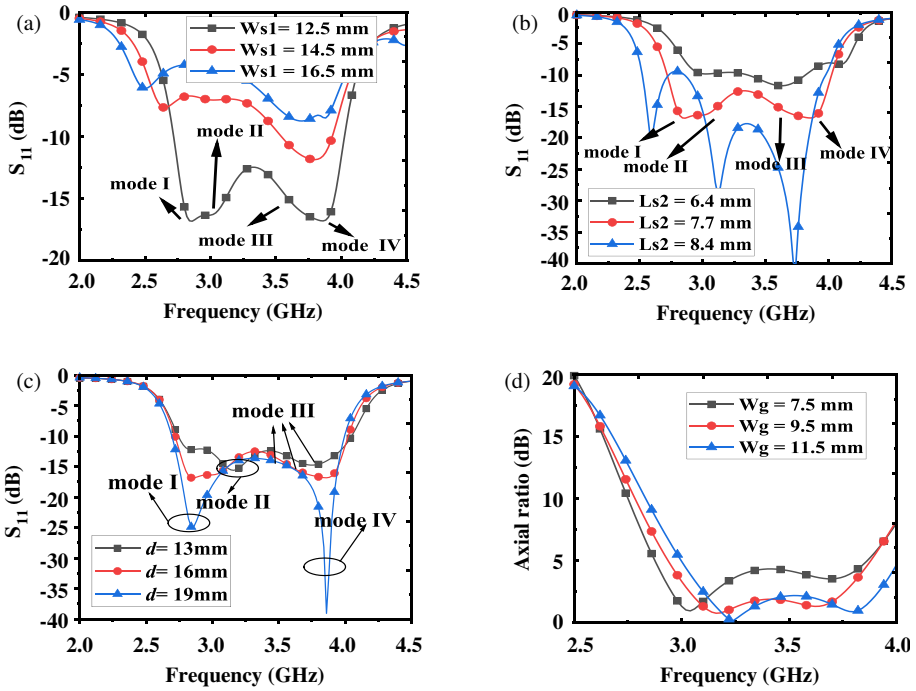

FIGURE 9. Simulation results of parametric analysis, (a) S_{11} with varying length of horizontal slot W_{s1}, (b) S_{11} with varying length of vertical slot L_{s2}, (c) S_{11} with varying height of DR d, (d) axial ratio with varying depth of slot of DR W_g.

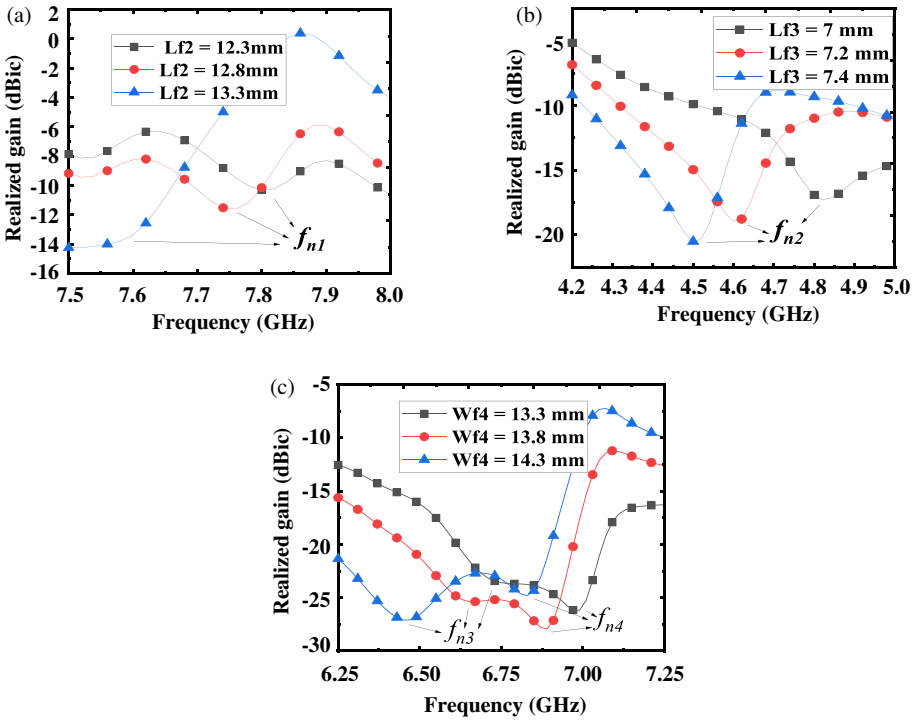

FIGURE 10. Simulation results of parametric analysis of realized gain, (a) with varying length of double-ended stub L_{f2}, (b) with varying length π-shaped stub of L_{f3}, (c) with varying length of transverse stub W_{f4}.

downward frequency shift as W_{f4} increases from 13.3 mm to 14.3 mm.

In summary, the resonant modes within the operating band can be independently tuned by adjusting the size of the DR and slot, while the radiation nulls in the stopband can be precisely positioned by modifying the corresponding sections of the feeding structure. Through coordinated parameter optimization, this approach enables an integrated design of a broadband circularly polarized (CP) antenna with wideband harmonic suppression.

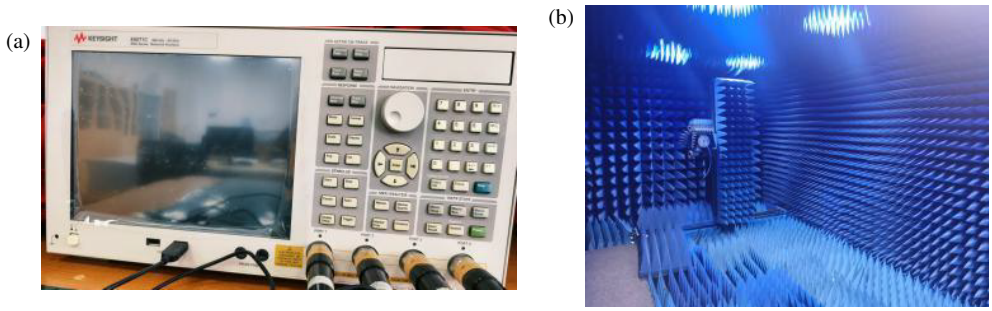

FIGURE 11. Hardware equipment used in measurement. (a) Vector network analyzer. (b) Microwave anechoic chamber.

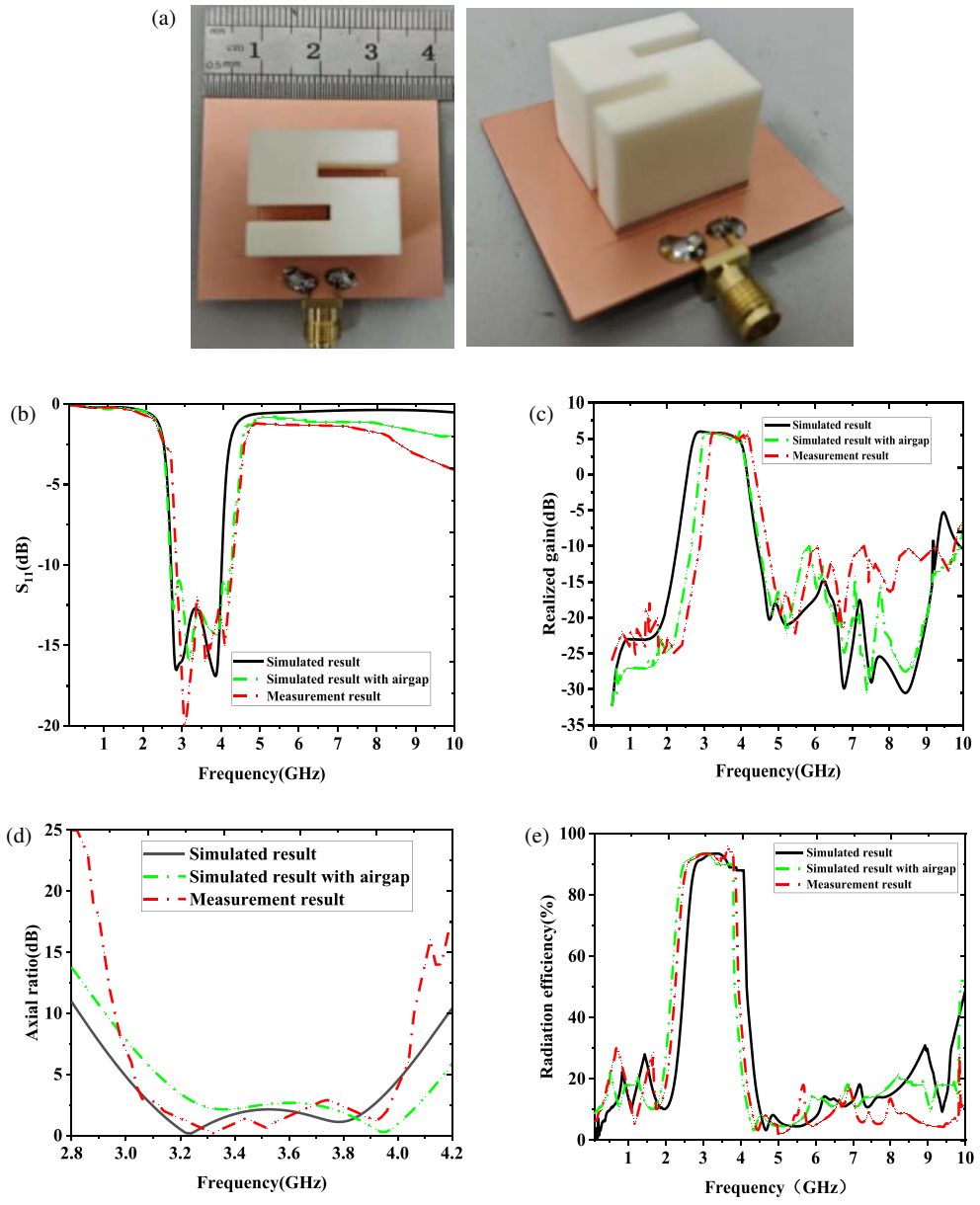

FIGURE 12. (a) View of the manufactured wideband CP DRA. (b) Simulation and measurement S_{11}. (c) Realized gain. (d) Axial ratio. (e) Radiation efficiency.

3. RESULTS AND DISCUSSION

A prototype is fabricated and measured to validate the antenna design. The dielectric resonator was adhered to the substrate. A 50-Ω SMA connector was employed to excite the antenna during measurement. The proposed antenna was primarily simulated using the electromagnetic simulation software ANSYS

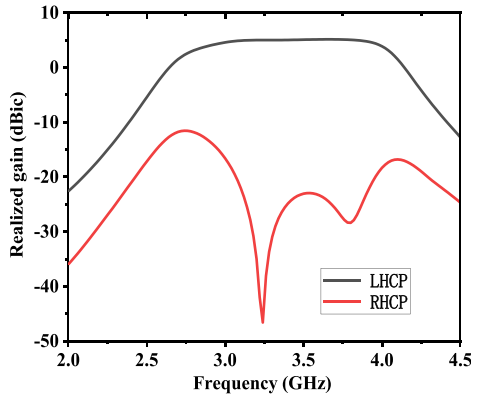

FIGURE 13. Comparison of LHCP and RHCP gains of the proposed antenna within the passband.

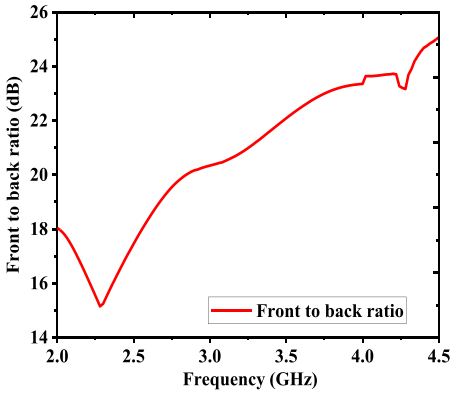

FIGURE 14. Front-to-back ratio of the proposed antenna within the passband.

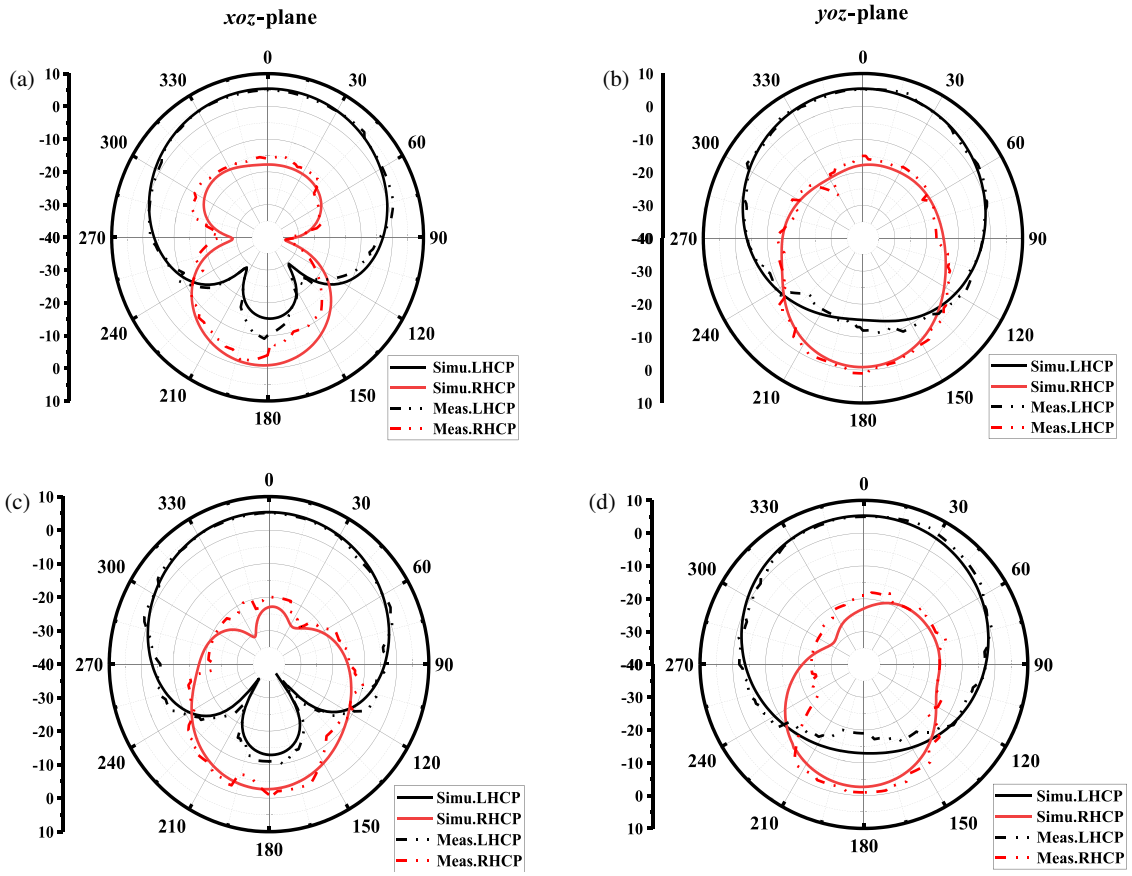

FIGURE 15. Radiation pattern of the CP DRA at axial ratio nulls. (a) Simulated and measurement result at 3.24 GHz. (b) Simulated and measurement result at 3.78 GHz.

Electronics High Frequency Structure Simulator (HFSS), and then verified through practical measurement using a vector network analyzer and microwave anechoic chamber, as shown in Fig. 11. Fig. 12 shows the fabricated structure and measured results of the proposed antenna. The measured results in Fig. 12(b) confirm the excitation of four operational modes: horizontal slot mode, orthogonal modes TE^{x}_{111} and TE^{y}_{111} of DR, and vertical slot mode. The measured ($S_{11} < -10$ dB) impedance bandwidth is 40.2%, in close agreement with the simulated 38.4%. In the measured results, the first two resonant modes merge into a single response due to a slight frequency shift induced by an assembly induced air gap between DR and substrate. Nevertheless, the measured realized gain shows good agreement with the simulation in trend, maintaining a flat gain within the passband while achieving a stopband up to $2.7f_0$ (where f_0 is the center frequency) with effective out-of-band suppression about 15 dB. Furthermore, as we can see in Fig. 12(e), the in-band radiation efficiency exceeds 90%, while the out-of-band radiation efficiency is below 25%, achieving good stopband rejection. Some discrepancy is

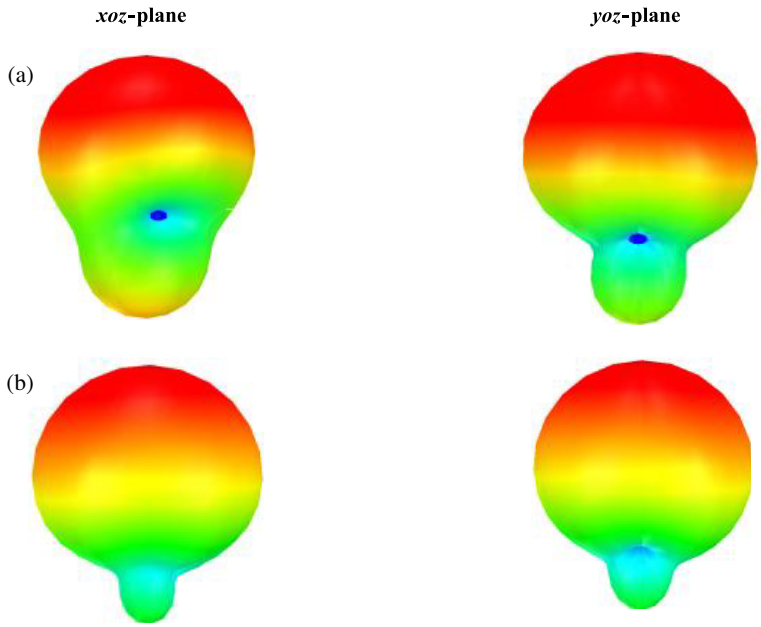

FIGURE 16. 3D radiation pattern of the CP DRA at axial ratio nulls, (a) at 3.24 GHz, (b) at 3.78 GHz.

TABLE 2. Comparison with previous CP and HS antenna.

Ref.	Impedance BW (dB)	Axial Ratio BW (dB)	f_0 (GHz)	Realized Gain (dBi/dBic)	Harmonic Suppression (dB)	Antenna Size ($\lambda_0 * \lambda_0 * \lambda_0$)
[2]	9.8%	9.2%	2.63	9.2	no	$0.7 * 0.7 * 0.03$
[14]	10.2%	\	6.78	8.59	$2.58f_0$	$0.95 * 0.95 * 0.17$
[15]	1%	1%	1.4	4.8	$2.1f_0$	$0.07 * 0.07 * 0.011$
[18]	7.1%	5.2%	3.53	6.45	$2.37f_0$	$0.75 * 0.67 * 0.028$
[22]	62.2%	24.2%	1.4	5.06	no	$0.5 * 0.5 * 0.13$
[23]	4.2%	\	1.8	6.8	$2.22f_0$	$0.63 * 0.63 * 0.055$
[25]	10%	\	2.6	5.6	$2.67f_0$	$0.35 * 0.35 * 0.074$
Proposed	40.2%	26.13%	3.58	5.3	$2.7f_0$	$0.48 * 0.48 * 0.19$

λ_0: free space wavelength at the center frequency. BW: bandwidth.

witnessed between the measured and simulated results, which is likely attributable to surface oxidation or SMA soldering, assembly tolerances. The axial ratio comparison between simulation and measurement is provided in Fig. 12(d). The measured axial ratio (AR) bandwidth is 26.13%, which is closely consistent with the simulated value of 24.8%. A consistent rightward frequency shift is observed across the S_{11}, realized gain, and AR characteristics. This shift is attributed to the inevitable air gap introduced by the adhesive used to mount the dielectric resonator (DR), which effectively lowers the surrounding dielectric constant and consequently increases the resonant frequency of DR. We have additionally performed simulations incorporating an air gap, in which the S_{11}, realized gain, axial ratio, and radiation efficiency are basically consistent with the explanation provided in the error analysis.

In addition, Fig. 13 presents the realized gains of LHCP and RHCP within the passband. The results show that the LHCP exceeds the RHCP by more than 20 dB, achieving good RHCP radiation. Fig. 14 shows the front-to-back ratio within the passband, where it can be observed that the front-to-back ratio is greater than 20 dB, achieving good forward radiation.

The radiation patterns at the axial ratio minimum frequency are presented in Fig. 15 for both simulation and measurement. The measured patterns are consistent with the simulated trends. The left-handed circular polarization (LHCP) characteristic exceeds the right-handed circular polarization (RHCP) characteristic by approximately 20 dB in the broadside direction, demonstrating effective LHCP radiation. Furthermore, Fig. 16 illustrates the 3D radiation patterns at four frequencies within the passband, demonstrating stable radiation performance. To further demonstrate the innovation of the design, Table 2 presents a comparison between this work and previous literature. Although the realized gain is slightly lower, it can be observed that desirable performance has been achieved in terms of wideband operation, circular polarization, and wide harmonic suppression. Meanwhile, the size of the antenna is moderate in comparison.

4. CONCLUSION

This paper presents a broadband CP DRA with integrated wideband harmonic suppression. The proposed design employs a branched slotline to simultaneously excite two pairs of orthogonal resonant modes: horizontal and vertical slot modes, and TE^{x}_{111} and TE^{y}_{111} modes of DR. This multi-mode excitation mechanism enables a wide overlapping impedance and AR bandwidth. Furthermore, a compact filtering feed network incorporating four tunable radiation nulls and a stepped-impedance resonator (SIR) structure achieves a wide stopband extending up to $2.7f_0$ with out-of-band suppression exceeding 15 dB. The prototype of the proposed antenna is fabricated and measured, and the simulated and experimental results are mutually corroborated, validating the design concept.

ACKNOWLEDGEMENT

This work is funded by the National Natural Science Foundation of China (No. 61901170) and the Key R&D Program of Jiangxi Province, China (Nos. 20261BCE310039, 20243BBG71030).

REFERENCES

[1] Liu, S., Z. Wang, and Y. Dong, "A compact filtering patch antenna with high suppression level and its CP application," *IEEE Antennas and Wireless Propagation Letters*, Vol. 22, No. 4, 769–773, Apr. 2023.

[2] Shi, T., R. Chai, X. Chen, M. Li, T. Zhang, and M.-C. Tang, "A low-profile, circularly polarized, metasurface-based antenna with enhanced bandwidth and stable high gain," *IEEE Antennas and Wireless Propagation Letters*, Vol. 22, No. 2, 253–257, Feb. 2023.

[3] Liu, Q., H. Yan, L. Zhu, Y. Tang, Y.-p. Lyu, and F. Huang, "Compact single-layer wideband CP antenna array with stable radiation and filtering performance using patch resonator and SIW cavity," *IEEE Antennas and Wireless Propagation Letters*, Vol. 24, No. 10, 3779–3783, Oct. 2025.

[4] Chen, C., "An ultraminiature circularly polarized microstrip patch antenna with MIM capacitors," *IEEE Antennas and Wireless Propagation Letters*, Vol. 22, No. 6, 1496–1500, Jun. 2023.

[5] Fang, C., X. Zhang, Y. Li, T. Yuan, Z. Quan, and S.-W. Wong, "Dual-circularly polarized reflectarray based on polarization selectivity of single-fed CP antenna element," *IEEE Transactions on Antennas and Propagation*, Vol. 73, No. 1, 647–652, Jan. 2025.

[6] Chen, Z. and J. Sui, "A self-decoupled circularly polarized microstrip antenna via cross-handed current cancellation," *IEEE Antennas and Wireless Propagation Letters*, Vol. 25, No. 1, 234–238, Jan. 2026.

[7] Xu, T., J.-F. Li, L.-H. Ye, D.-L. Wu, and G. Zhang, "A wideband circularly polarized filtering patch antenna with strip network," *IEEE Antennas and Wireless Propagation Letters*, Vol. 22, No. 12, 2826–2830, Dec. 2023.

[8] Chu, C., Y. Li, J. Wang, Y. Guo, and W. Wu, "A rectangular patch antenna with wideband harmonic suppression," *IEEE Antennas and Wireless Propagation Letters*, Vol. 22, No. 12, 3102–3106, Dec. 2023.

[9] Huang, R., Y. Luo, N. Yan, W. An, K. Ma, and W. Lin, "A differential multipoint coupled-fed harmonic suppression patch antenna with a single-layer and filter-free structure," *IEEE Antennas and Wireless Propagation Letters*, Vol. 23, No. 12, 4473–4477, Dec. 2024.

[10] Chu, C., M. Wang, J. Wang, Y. Guo, and W. Wu, "A new design of filtering patch antennas with enhanced bandwidth and harmonic suppression," *IEEE Transactions on Antennas and Propagation*, Vol. 71, No. 7, 6120–6125, Jul. 2023.

[11] Prasad, C. S., "Wide range of harmonics suppression of a semicircular patch antenna using shorting vias," *IEEE Antennas and Wireless Propagation Letters*, Vol. 24, No. 8, 2173–2176, Aug. 2025.

[12] Huang, F., L. Zhu, and H. Zhang, "Study on a multi-point differential feeding strategy for design of filtering patch antennas with stopband enhancement," *IEEE Transactions on Antennas and Propagation*, Vol. 70, No. 12, 11 293–11 300, Dec. 2022.

[13] Li, D., Y. Ma, K.-Z. Hu, Z. Chen, M. Xiang, and M.-C. Tang, "A differentially-fed dual-polarized filtering antenna with wide harmonic suppression for high-integration RF front-ends," *IEEE Antennas and Wireless Propagation Letters*, Vol. 25, No. 2, 511–515, Feb. 2026.

[14] Hu, Y., H. Sun, X. Wu, and G. Wang, "A high-gain, wide-stopband filtering antenna based on cross-coupling for mobile applications," *IEEE Antennas and Wireless Propagation Letters*, Vol. 23, No. 8, 2346–2350, Aug. 2024.

[15] Yun, Y., Y. Liu, Z. Wu, and H. Lennerstad, "Harmonic suppression and size reduction of a low-profile CP patch antenna by using nondegenerate modes," *IEEE Antennas and Wireless Propagation Letters*, Vol. 21, No. 3, 456–460, Mar. 2022.

[16] Liu, N.-W., L. Zhu, Z.-X. Liu, G. Fu, and Y. Liu, "Design approach for low-profile tri-polarization patch antenna with simultaneous harmonic suppression," *IEEE Transactions on Antennas and Propagation*, Vol. 70, No. 4, 2401–2410, Apr. 2022.

[17] Xu, Y., S. Gong, and T. Hong, "Circularly polarized slot microstrip antenna for harmonic suppression," *IEEE Antennas and Wireless Propagation Letters*, Vol. 12, 472–475, 2013.

[18] Hu, Y., Y. Wu, G. Wang, and X. Wu, "A circularly polarized, highly selective, harmonic-suppressed filtering antenna for 5G application," *IEEE Antennas and Wireless Propagation Letters*, Vol. 23, No. 12, 4308–4312, Dec. 2024.

[19] Elahi, M., A. Altaf, Y. Yang, K.-Y. Lee, and K. C. Hwang, "Circularly polarized dielectric resonator antenna with two annular vias," *IEEE Access*, Vol. 9, 41 123–41 128, 2021.

[20] Kumari, R., R. K. Gangwar, and R. K. Chaudhary, "Investigation on rotated rectangular slots to improve the circular polarization in cylindrical dielectric resonator antenna," *IEEE Access*, Vol. 9, 97 327–97 336, 2021.

[21] Kiyani, A., N. Nasimuddin, R. M. Hashmi, A. A. Baba, S. M. Abbas, K. P. Esselle, and A. Mahmoud, "A single-feed wideband circularly polarized dielectric resonator antenna using hybrid technique with a thin metasurface," *IEEE Access*, Vol. 10, 90 244–90 253, 2022.

[22] Liu, S., H. Liu, Y. Zeng, Z. Wang, S. Fang, and X. Sun, "Wideband circularly polarized dielectric resonator antenna with wide overlapped axial-ratio and half-power beamwidths," *IEEE Antennas and Wireless Propagation Letters*, Vol. 23, No. 8, 2376–2380, Aug. 2024.

[23] La, D.-S., H. Liu, R.-L. Wang, K. Tian, and M.-J. Qu, "A wide stopband filtering DDPA with metal vias and metal strips," *IEEE Transactions on Antennas and Propagation*, Vol. 72, No. 3, 2843–2848, Mar. 2024.

[24] Hu, P. F., Y. M. Pan, X. Y. Zhang, and S. Y. Zheng, "Broadband filtering dielectric resonator antenna with wide stopband," *IEEE Transactions on Antennas and Propagation*, Vol. 65, No. 4, 2079–2084, Apr. 2017.

[25] Tang, H., C. Tong, and J.-X. Chen, "Differential dual-polarized filtering dielectric resonator antenna," *IEEE Transactions on Antennas and Propagation*, Vol. 66, No. 8, 4298–4302, Aug. 2018.

[26] Liu, X., K. W. Leung, and N. Yang, "Frequency reconfigurable filtering dielectric resonator antenna with harmonics suppression," *IEEE Transactions on Antennas and Propagation*, Vol. 69, No. 6, 3224–3233, Jun. 2021.

[27] Vahora, A. and K. Pandya, "Implementation of cylindrical dielectric resonator antenna array for Wi-Fi/wireless LAN/satellite applications," *Progress In Electromagnetics Research M*, Vol. 90, 157–166, 2020.